Environmental Science: Atmospheres

ROYAL SOCIETY OF CHEMISTRY

PAPER

View Article Online
View Journal | View Issue

Cite this: *Environ. Sci.: Atmos.*, 2025, **5**, 998

Optimizing stratospheric aerosol lifetime and albedo through particle morphology and refractive index

Benjamin Vennes,[a] Alison Bain,[b] James F. Davies[c] and Thomas C. Preston *[ad]

Stratospheric aerosol injection (SAI) has been proposed as a geoengineering approach to temporarily offset global warming by increasing Earth's albedo. Here, we utilize light scattering calculations to examine how introducing solid aerosol particles into the stratosphere can enhance the Bond albedo, a key metric linking reflectivity directly to radiative forcing. We explore how particle size, refractive index (both real and imaginary components), and morphology (core–shell configurations) affect single scattering albedo, phase function, and the resulting integrated solar reflectivity. Our results show how the optimal aerosol size is governed by matching the wavelength of dipolar resonances with the peak of incoming solar spectral irradiance. We also examine how dispersion, absorption, and size distribution affect the extent of the Bond albedo enhancement and radiative forcing. Coated particles are also studied, and we find that very thin lower-index coatings can spoil albedo enhancement (*e.g.*, layers of water or sulfuric acid that are only a few nanometres thick). Conversely, designing core–shell particles with a thin, higher-index shell and a low-density core can retain high reflectivity while substantially reducing particle mass and settling velocity, potentially extending the stratospheric residence time. The framework discussed here is versatile, readily extending to systems beyond homogeneous spherical particles, and it provides a straightforward means of comparing candidate SAI materials while guiding future laboratory studies, work on particle design, field experiments, and climate model parameterizations to assess the viability and risks of stratospheric aerosol geoengineering.

Received 19th February 2025
Accepted 11th August 2025

DOI: 10.1039/d5ea00026b

rsc.li/esatmospheres

Environmental significance

Stratospheric aerosol injection (SAI) is one of the most debated proposed climate interventions. Uncertainties in SAI remain due to aerosol–radiation interactions and stratospheric chemistry. This work demonstrates how engineering aerosol particles, particularly by tuning their refractive index and morphology, can significantly improve Earth's reflectivity and prolong stratospheric residence times, thereby increasing their geoengineering efficacy. This study also demonstrates that coatings can either diminish or enhance scattering and provide a practical framework for selecting and designing future SAI materials. Such advances could reduce the frequency of injections needed, lowering operational costs and environmental risks associated with continuous particle releases. Overall, these results offer a clearer path toward more targeted SAI strategies and underscore the need for careful experimental validation and climate model integration with SAI implementation.

1 Introduction

Strongly motivated by the cooling observed after major volcanic eruptions, stratospheric aerosol injection (SAI) has been proposed as a temporary measure to combat the increased global temperatures associated with climate change. Volcanic eruptions can release large quantities of SO_2 into the stratosphere, which form sulphate aerosol after oxidation. This increase in stratospheric aerosol loading perturbs Earth's radiative balance by scattering more solar radiation, cooling the troposphere.[1,2] The Mount Pinatubo eruption in June 1991 introduced 1.7×10^{10} kg of SO_2 into the atmosphere, leading to a global cooling effect of 0.5 K over 2–3 years.[3] This has motivated scientists to apply climate and circulation models to predict the potential cooling and other impacts of using sulphate aerosol for stratospheric aerosol injection.[4–19]

Sulphate aerosol particles are typically concentrated H_2SO_4–H_2O solutions due to their strong hygroscopicity and exhibit a moderately high real part of the refractive index (RI) across the solar-visible range (about 1.43 at 533 nm for 70 wt% H_2SO_4).[20] They absorb minimally in the visible region, but increasing

[a]*Department of Chemistry, McGill University, Montreal, Quebec, Canada. E-mail: thomas.preston@mcgill.ca*
[b]*Department of Chemistry, Oregon State University, Corvallis, Oregon, USA*
[c]*Department of Chemistry, University of California Riverside, Riverside, California, USA*
[d]*Department of Atmospheric and Oceanic Sciences, McGill University, Montreal, Quebec, Canada*

absorption through the infrared portion of the solar spectrum may cause warming in the stratosphere, altering atmospheric dynamics.[21] Sulphate may also affect ozone concentrations in the stratosphere. The injection of sulphate aerosol by Mount Pinatubo led to a reduction in total ozone of up to 20% in some regions and an average of 6–8% reduction in column ozone in the tropics, resulting in increased surface UV exposure.[3] Similar magnitudes of ozone reduction have been predicted for sulphate SAI interventions.[4,8,12,22] To alleviate some of these negative effects, solid aerosol particles have been proposed as viable candidates for SAI, with the potential to reduce the impact on ozone, produce less stratospheric heating, and result in less forward scattering than sulphate aerosols, for the same radiative forcing.[23]

A range of alternative materials to produce solid aerosol particles are now being explored for SAI.[6,23–28] Materials with high real parts of the RI in the visible and near-infrared spectrum, such as diamond, calcite, alumina, titania, silicon carbide, and cubic zirconium, will scatter radiation more efficiently than sulphate.[21,23,24] Furthermore, many of these materials also have lower imaginary parts of the RI than sulphate throughout the infrared region, leading to less stratospheric warming.[24] They may also exhibit some advantages in terms of the chemistry of the stratosphere, with calcite shown to have less impact on atmospheric ozone compared to sulphate,[29] although alumina particles may have a strong depleting effect.[26,30] The impact of solid aerosol particles on other trace gases in the stratosphere, such as HCl, is less well-constrained.[27,31,32] A further limitation of solid particles compared to sulphate is their increased density, leading to shorter stratospheric residence times and requiring more frequent injections to maintain cooling.[23] As an alternative, hybrid particles with novel particle morphologies could be engineered to reduce the density and increase atmospheric lifetimes, while maintaining the beneficial optical and chemical properties of solid particles.[33,34]

At the present time, available data on the optical properties of candidate materials may not be sufficient to accurately predict their scattering efficiency in the stratosphere. Furthermore, at the point of injection, aerosol will be highly concentrated and may undergo aggregation. If this occurs, the scattering properties, which depend both on geometry and RI, will be impacted.[23] Additionally, under stratospheric conditions, naturally present sulphate and water may condense onto the surface of solid particles. A layer of liquid will alter the optical properties of particles. These changes in optical properties, as well as the reduced stratospheric lifetime associated with more massive particles, will impact the effectiveness of solid aerosol for geoengineering.[35]

It is computationally intensive to incorporate a full consideration of chemistry, transport, particle interactions, and optical processes in a climate model, and we lack sufficient physicochemical and optical data to fully predict the impact of SAI in the atmosphere over the lifetime of the intervention. However, a simple way to assess the impact of SAI candidates on radiative forcing is to calculate the change in the Bond albedo due to the addition of aerosol particles. The Bond albedo is a measure of the reflectivity of an object and SAI methods aim to increase the albedo by an amount that offsets the radiative forcing impact of CO_2. In this work, we apply a straightforward optical model to calculate the Bond albedo and explore the resulting global radiative effects of particles with a variety of morphologies and optical properties. We also assess the impact of the morphology on the lifetime of particles in the atmosphere, an important consideration for the long-term effectiveness of an SAI candidate.

2 Theory

We consider the change in Bond albedo, ΔA, arising from a layer of homogeneously distributed particles in the stratosphere. The analysis assumes that no scattering occurs above the introduced layer, and that photons within the layer experience at most one scattering event. Under these conditions, ΔA can be approximated as[21]

$$\Delta A = \frac{2}{\pi}\left[\int_{\lambda_1}^{\lambda_2} \omega\tau\bar{\beta}E_\lambda^{\mathrm{sun}}\mathrm{d}\lambda\right]\Big/\left[\int_{\lambda_1}^{\lambda_2} E_\lambda^{\mathrm{sun}}\mathrm{d}\lambda\right], \quad (1)$$

where ω is the single scattering albedo, τ is the optical depth, $\bar{\beta}$ is the isotropic upscatter fraction, E_λ^{sun} is the solar spectral irradiance, and the integration is performed over wavelengths λ between λ_1 and λ_2. Here, the incident E_λ^{sun} on the layer being considered is taken to be the same as the top-of-atmosphere (TOA) solar spectral irradiance.[36]

The single scattering albedo ω expresses the fraction of incident light that is scattered (rather than absorbed) by a single particle and can be defined in terms of efficiencies as[37]

$$\omega = \frac{Q_{\mathrm{sca}}}{Q_{\mathrm{ext}}}, \quad (2)$$

where Q_{sca} and Q_{ext} are the scattering and extinction efficiencies, respectively. The optical depth τ quantifies the attenuation of light as it travels through a column of monodisperse particles:[37]

$$\tau = NC_{\mathrm{ext}}H, \quad (3)$$

where N is the number concentration of particles, C_{ext} is the single particle extinction cross-section, and H is the height of the column. Following Pope *et al.*,[21] these values are chosen so that the volume of aerosol per unit volume of air is kept at the dimensionless value of $(4\pi/3) \times 10^{-12}$. Therefore, for an aerosol radius of 1 μm, this corresponds to a number density of 1 cm^{-3}. We set $H = 1$ km in all calculations. Because the optical depth primarily depends on the total aerosol volume along the path, a layer of 10 km in depth with a particle number concentration of 0.1 cm^{-3} has the same radiative effect (in terms of ΔA) as a layer of 1 km depth with 1 cm^{-3}, since both yield the same total aerosol volume.[21]

The isotropic upscatter fraction $\bar{\beta}$ denotes the fraction of scattered light directed upwards, averaged over the solar incidence angle. It can be reduced to the single integral[38]

$$\bar{\beta} = \frac{1}{2\pi}\int_0^{\pi} \theta P(\theta)\sin\theta\mathrm{d}\theta, \quad (4)$$

where $P(\theta)$ is the phase function. For unpolarized light, the Mie phase function is related to the amplitude scattering matrix elements by[39]

$$P(\theta) = \frac{|S_1(\theta)|^2 + |S_2(\theta)|^2}{2\pi x^2 Q_{sca}}, \quad (5)$$

where $S_1(\theta)$ and $S_2(\theta)$ are the scattering amplitudes and $x = 2\pi r/\lambda$ is the dimensionless size parameter (with r the particle radius and λ the wavelength of light). The scattering amplitudes are summations over the mode number l:

$$S_1(\theta) = \sum_{l=1}^{\infty} \frac{2l+1}{l(l+1)}[b_l \pi_l(\cos\theta) + a_l \tau_l(\cos\theta)], \quad (6)$$

$$S_2(\theta) = \sum_{l=1}^{\infty} \frac{2l+1}{l}[a_l \pi_l(\cos\theta) + b_l \tau_l(\cos\theta)]. \quad (7)$$

The Mie scattering coefficients a_l (transverse electric modes) and b_l (transverse magnetic modes) depend on the particle's optical (*e.g.*, complex refractive index) and geometrical (*e.g.*, size parameter) properties, while the functions π_l and τ_l determine the angular dependence of the scattering, whose definition can be found elsewhere.[39] The extinction and scattering efficiencies can also be expressed in terms of these Mie coefficients:

$$Q_{ext} = \frac{2}{x^2} \sum_{l=1}^{\infty} (2l+1)\mathrm{Re}(a_l + b_l), \quad (8)$$

$$Q_{sca} = \frac{2}{x^2} \sum_{l=1}^{\infty} (2l+1)\left(|a_l|^2 + |b_l|^2\right). \quad (9)$$

For a homogeneous dielectric sphere, the Mie scattering coefficients are expressed as

$$a_l = \frac{m\psi_l'(mx)\psi_l(x) - \psi_l'(x)\psi_l(mx)}{m\psi_l'(mx)\xi_l(x) - \xi_l'(x)\psi_l(mx)}, \quad (10)$$

$$b_l = \frac{m\psi_l'(x)\psi_l(mx) - \psi_l'(mx)\psi_l(x)}{m\xi_l'(x)\psi_l(mx) - \psi_l'(mx)\xi_l(x)}, \quad (11)$$

where $m = n + ik$ is the complex refractive index of the spherical particle and the Riccati–Bessel functions $\psi_l(z)$ and $\xi_l(z)$ relate to the spherical Bessel functions of the first and third kind by $\psi_l(z) = zj_l(z)$ and $\xi_l(z) = zh_l(z)$.

When calculating the isotropic upscatter fraction, we insert the scattering amplitudes from eqn (6) and (7) into eqn (4), assuming the unpolarized form of the phase function given by eqn (5). This results in the following double sum over the mode number l:

$$\bar{\beta} = \frac{1}{2\pi^2 x^2 Q_{sca}} \sum_{l=1}^{\infty} \frac{2l+1}{l(l+1)} \sum_{l'=1}^{\infty} \frac{2l'+1}{l'\left(l'+1\right)} \Big[\left(b_l b_{l'}^* + a_l a_{l'}^*\right) {I_{ll'}}^1 + \left(a_l b_{l'}^* + b_l a_{l'}^*\right) {I_{ll'}}^2\Big], \quad (12)$$

where $I_{ll'}^{(1,2)}$ are integrals defined by

$${I_{ll'}}^1 = \int_0^{\pi} \theta\left(\pi_l \pi_{l'} + \tau_l \tau_{l'}\right) \sin\theta \mathrm{d}\theta, \quad (13)$$

$${I_{ll'}}^2 = \int_0^{\pi} \theta\left(\pi_l \pi_{l'} + \tau_l \tau_{l'}\right) \sin\theta \mathrm{d}\theta. \quad (14)$$

These integrals do not depend on particle parameters and can therefore be computed numerically once, tabulated, and subsequently used for calculating the isotropic upscatter fraction as a function of size parameter and refractive index. Fig. S1 compares calculations performed using the method described here with those using the commonly employed Henyey–Greenstein phase function to determine $\bar{\beta}$.[38] For the large refractive indices and small particle sizes relevant to SAI, differences in the resulting ΔA between the two methods are only a few percent. Furthermore, once the integrals $I_{ll'}^{(1,2)}$ have been tabulated, the practical difference in computational efficiency between the methods was found to be relatively minor for the systems studied here (the Henyey–Greenstein method was slightly faster). Overall, in terms of both speed and accuracy, either method is satisfactory for typical SAI studies.

The formalism presented here can be extended to spherically symmetric layered particles (*e.g.*, core–shell configurations) by using the appropriate forms of a_l and b_l.[40] For non-spherical aerosols, more extensive modifications are required, as random orientation relative to incoming solar radiation alters both cross sections and phase functions. In the T-matrix framework, these effects can be accounted for analytically by computing orientation-averaged cross sections and phase functions from the T-matrix elements.[41] However, non-spherical aerosols are outside the scope of this work and are not considered further.

3 Results and discussion

The Bond albedo quantifies the total radiation reflected from Earth as a fraction of the total incident radiation and, thus, is restricted to values between 0 and 1. A Bond albedo of 0 indicates an object that absorbs all radiation, while a value of 1 indicates an object that reflects all incoming radiation. The average Bond albedo of Earth is approximately 0.294,[42] and although the connection between changes in radiative forcing due to Bond albedo and a CO_2-equivalent warming effect is not always straightforward,[43] it is estimated that the Bond albedo would need to increase by 0.018 to offset the effect of doubling CO_2.[44] As Bond albedo directly influences Earth's energy balance, the change in Bond albedo, ΔA, serves as a useful quantitative metric for assessing how modifications to Earth's reflectivity, including geoengineering interventions like SAI, impact radiative forcing.[21] Relevant here, ΔA enables direct comparisons between different scattering materials for SAI.

The correspondence between ΔA and the globally and annually averaged radiative forcing, $\Delta\bar{F}$, can be determined using a multiple reflection model[37,45,46] for TOA forcing. When the wavelength range in eqn (1) spans the entire solar spectrum and the aerosol is weakly absorbing ($\omega \sim 1$), ΔA and $\Delta\bar{F}$ have the negative linear relationship

$$\Delta\bar{F} = -k_F \Delta A \quad (15)$$

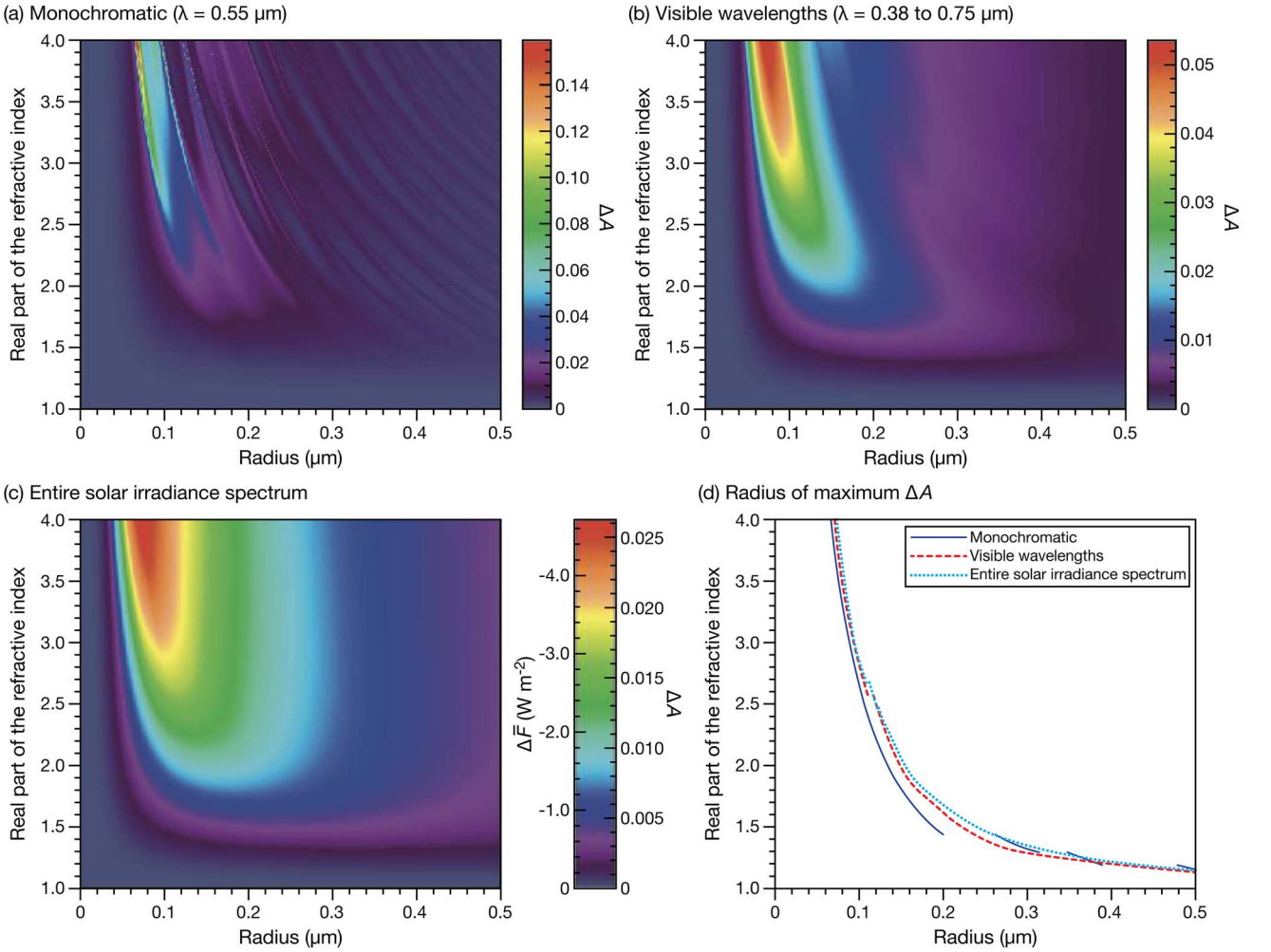

Fig. 1 Change in the Bond albedo, ΔA, as a function of particle radius and the real part of the refractive index. In all calculations, the imaginary part of the refractive index is set to 10^{-9}. In (a), ΔA is calculated at $\lambda = 0.55$ μm, in (b) across $\lambda = 0.38$–0.75 μm, and in (c) over the full solar spectrum. The color bar in (c) shows values for both ΔA and the globally averaged radiative forcing, $\Delta\bar{F}$. In (d), the position of the maximum ΔA for (a–c) is shown.

where k_F is given by:

$$k_F = \frac{\pi}{2} D F_0 T_a^2 (1 - A_c)(1 - R_s)^2. \quad (16)$$

Here, D is the fractional daylength, F_0 is the incident solar flux at the TOA (often referred to as the solar constant), T_a is the fractional transmittance of the atmosphere above the aerosol layer, A_c is the fractional cloud coverage, and R_s is the albedo of the underlying Earth's surface. The parameters in k_F represent geophysical variables influencing the magnitude of radiative forcing, whereas ΔA contains the aerosol-specific properties, including optical depth, single-scattering albedo, upscatter fraction, and aerosol microphysical properties such as size distribution and composition. The solar constant, F_0, is determined by integrating the solar irradiance E_λ^{sun} over the entire solar spectrum, which yields an approximate value of 1370 W m^{-2}. If we set $D = 0.5$ and take the remaining variable values from Table S24.2 of ref. 37 ($T_a = 0.76$, $A_c = 0.6$, and $R_s = 0.15$), then for weakly absorbing aerosol, $\Delta\bar{F} = -179.6\Delta A$ (in W m^{-2}).

Fig. 1 illustrates the variation in ΔA for spherical particles as a function of the real part of the RI and particle radius. The imaginary part of the RI is set to an extremely low value ($k = 10^{-9}$) and has no effect on the results. The chosen range for the real part of the refractive index spans the values observed for most of the common SAI candidate materials (Fig. S2a). In Fig. 1a, where ΔA is calculated at a single wavelength ($\lambda = 0.55$ μm), distinct Mie resonances appear as sharp ridges across the heatmap. These resonances arise due to the interaction of light with the spherical particles at specific size-to-wavelength ratios. However, these resonances are highly sensitive to wavelength and are smoothed out when ΔA is calculated over a range of wavelengths, as shown in Fig. 1b and c, where they no longer appear. Fig. 1b considers visible wavelengths ($\lambda = 0.38$–0.75 μm), while Fig. 1c incorporates the full solar spectrum. Additionally, the magnitude of ΔA decreases from Fig. 1a–c as the averaging over broader wavelength ranges reduces the albedo change, and it is clear that considering only visible wavelengths when calculating ΔA is inaccurate. Fig. 1c also contains $\Delta\bar{F}$

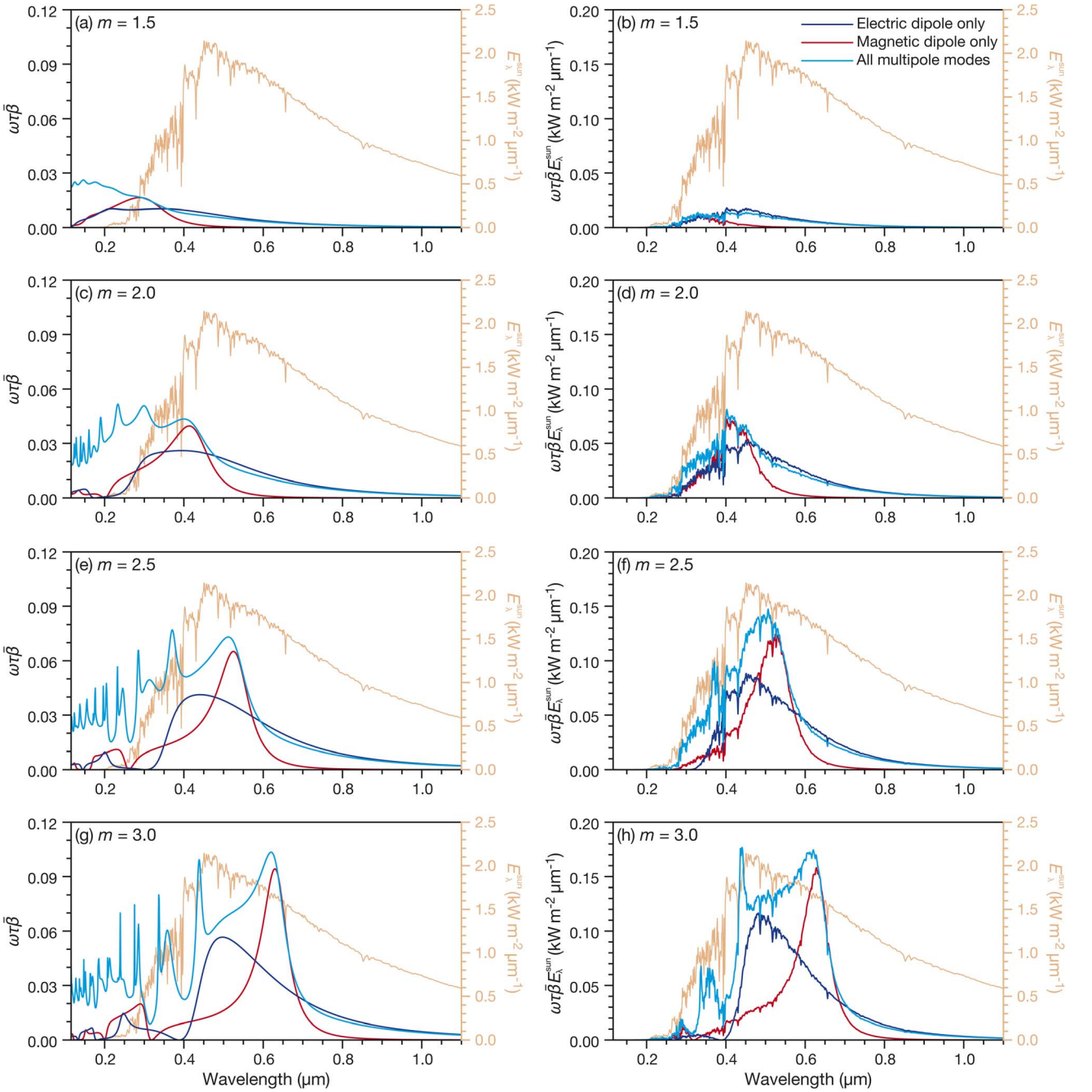

Fig. 2 Panels (a), (c), (e), and (g) show the upscatter optical depth, $\omega\tau\bar{\beta}$, while panels (b), (d), (f), and (h) show the upscattered solar spectral irradiance, $\omega\tau\bar{\beta}E_\lambda^{\text{sun}}$, all plotted as a function of wavelength for different refractive indices at a fixed particle radius $r = 0.10$ μm. The chosen refractive indices are $m = 1.5$ for (a and b), 2.0 for (c and d), 2.5 for (e and f), and 3.0 for (g and h). In each panel, curves are shown for calculations performed using (i) only the electric-dipole contribution, (ii) only the magnetic-dipole contribution, and (iii) all multipole modes (the full calculation). The solar spectral irradiance, E_λ^{sun}, is also included in all panels for comparison.

calculated using eqn (15) and the geophysical variables listed above. This directly quantifies the radiative impact (in W m^{-2}) associated with the changes in Bond albedo (ΔA) resulting from different particle properties. The peak values for $\Delta\bar{F}$ shown in Fig. 1c reach approximately -5.0 W m^{-2}, indicating substantial theoretical cooling potential. This magnitude exceeds the $+3.93 \pm 0.47$ W m^{-2} assessed by the IPCC AR6 as the effective radiative forcing from doubled CO_2.[47] However, the large forcing values in Fig. 1c arise under idealized assumptions regarding both particle morphology (monodisperse, perfectly spherical) and optical properties (high real refractive indices that have no wavelength dependence and negligible absorption). As will be subsequently shown, deviations from these assumptions reduce the magnitude of this predicted radiative forcing. Finally, Fig. 1d shows the particle radius at which ΔA reaches its

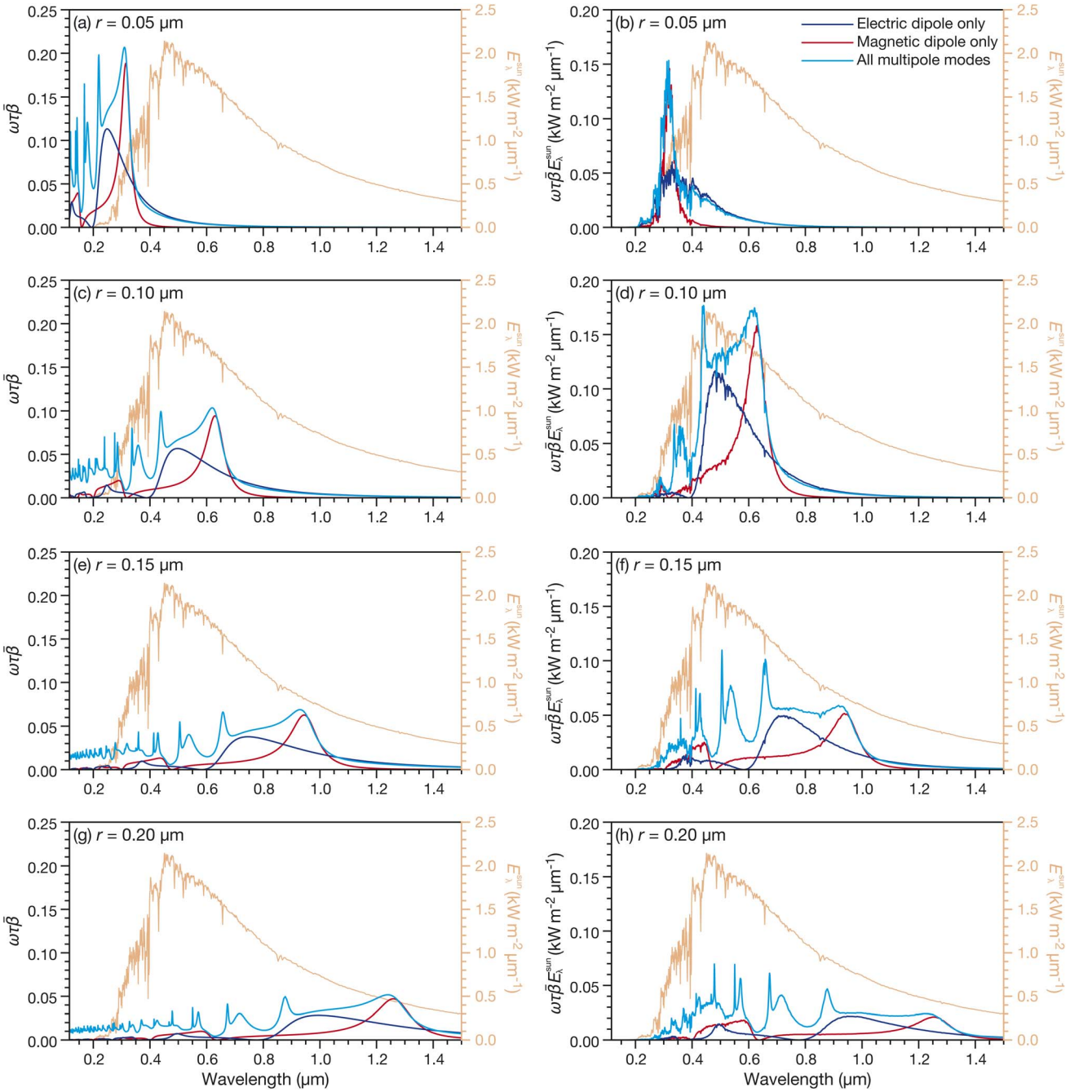

Fig. 3 Panels (a), (c), (e), and (g) show the upscatter optical depth, $\omega\tau\bar{\beta}$, while panels (b), (d), (f), and (h) show the upscattered solar spectral irradiance, $\omega\tau\bar{\beta}E_\lambda^{\text{sun}}$, all plotted as a function of wavelength for different particle radii at a fixed refractive index $m = 3$. The chosen radii are $r = 0.05$ μm for (a and b), 0.10 μm for (c and d), 0.15 μm for (e and f), and 0.20 μm for (g and h). In each panel, curves are shown for calculations performed using (i) only the electric-dipole contribution, (ii) only the magnetic-dipole contribution, and (iii) all multipole modes (the full calculation). The solar spectral irradiance, E_λ^{sun}, is also included in all panels for comparison.

maximum value of RI. While the locations are similar for high refractive indices, differences emerge at lower RI values.

Fig. 2 examines the wavelength dependence of the integrand in eqn (1) at a fixed particle radius of 0.10 μm and imaginary part of the RI set to zero. In addition to the standard calculation (labeled "All multipole modes"), we perform separate calculations using only b_1 or only a_1, thereby isolating the magnetic and electric dipole modes, respectively. This is done to highlight the role that these two specific modes play in the scattering process. Panels (a), (c), (e), and (g) show the upscatter optical depth, $\omega\tau\bar{\beta}$, which determines what fraction of light is reflected by the aerosol layer at each wavelength. For a real part of the RI of 1.5 (Fig. 2a), $\omega\tau\bar{\beta}$ is relatively small and primarily significant in the ultraviolet region. As the real part of the RI increases (Fig. 2c, e, and g), distinct Mie resonances appear as sharp peaks in the ultraviolet, while broad electric and

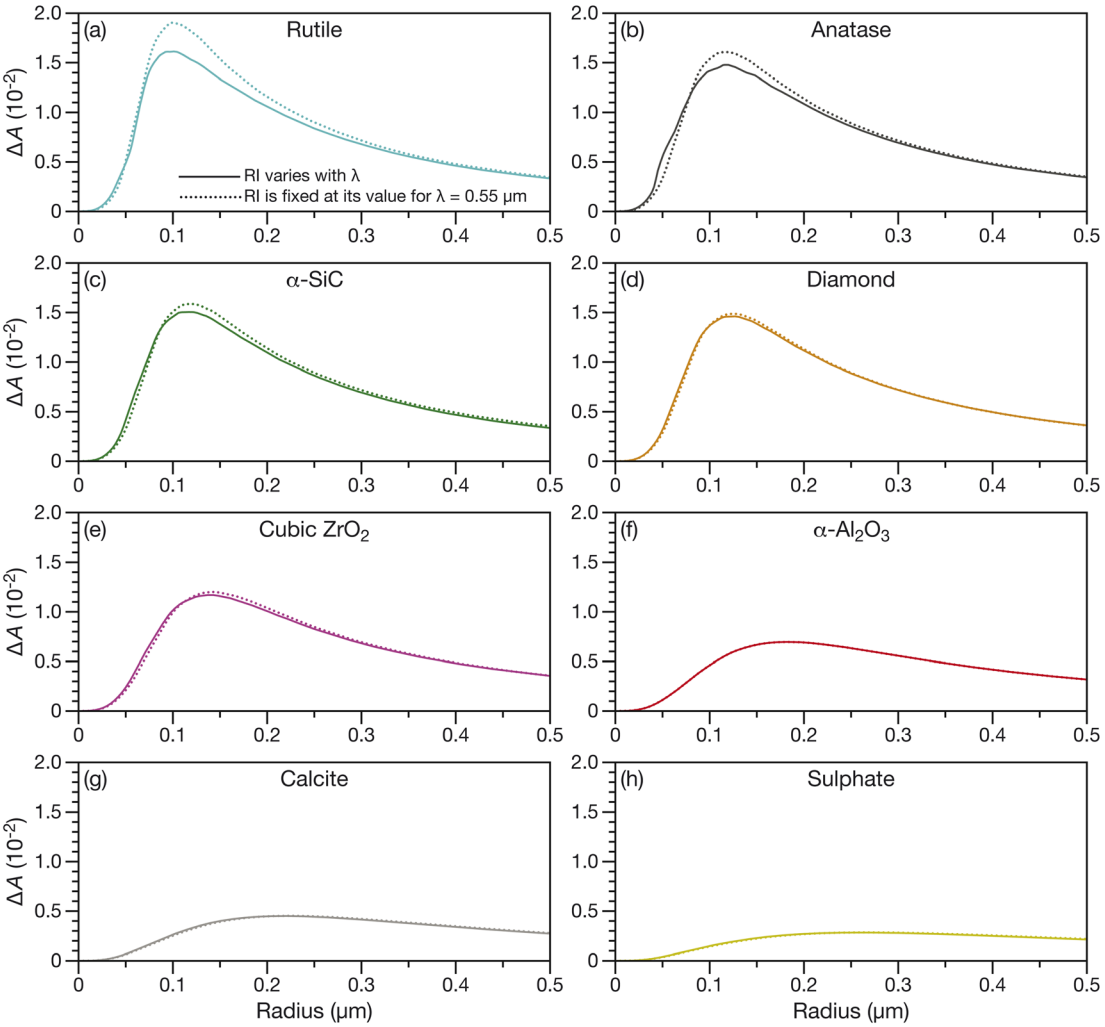

Fig. 4 Change in the Bond albedo, ΔA, as a function of particle radius for (a) rutile, (b) anatase, (c) α-SiC, (d) diamond, (e) cubic ZrO_2, (f) α-Al_2O_3, (g) calcite, and (h) sulphate. When calculating ΔA for these materials, the wavelength-dependent complex refractive index values between 0.2 and 3.00 μm were taken from Fig. 1 in ref. 24 and are also shown in Fig. S2.

magnetic dipolar modes dominate in the visible range. As the real part of the RI becomes large (*e.g.*, Fig. 2g where it is 3.0), the particle behaves as a high-permittivity dielectric resonator at visible wavelengths. Such resonators are characterized by strong light confinement and low energy losses.[48–50] Once a resonant mode (here, the electric or magnetic dipole) is confined, cross-sections increase, raising the upscatter optical depth. Another important factor is the angular distribution of the scattered light, which directly affects the isotropic upscatter fraction, $\bar{\beta}$. Panels (b), (d), (f), and (h) of Fig. 2 show the upscatter solar spectral irradiance, $\omega\tau\bar{\beta}E_\lambda^{\text{sun}}$. Integrating this quantity over all wavelengths yields the total reflected power. Because solar irradiance peaks in the visible region, the dominant contribution to the Bond albedo arises from the electric and magnetic dipolar resonances excited there.

Fig. 3 illustrates how particle size influences these resonances at a fixed RI of $m = 3$. At a smaller radius of 0.05 μm (Fig. 3a), the dipolar resonances lie in the near-ultraviolet, whereas at larger radii (Fig. 3c, e, and g) they shift into the visible and eventually into the near-infrared. In Fig. 3b and d, the reflected power peaks first in the near-ultraviolet and then in the visible, where the electric and magnetic dipolar resonances yield the largest increases in Bond albedo. Fig. 3d is notable because a particle radius of $r = 0.10$ μm is frequently chosen in SAI proposals as being optimal for reflectivity. We see that the reason why this size is optimal is because it aligns the electric and magnetic dipole modes with the peak of the solar spectral irradiance in the visible region. For larger particle sizes (Fig. 3f and h), the dipolar modes lie outside the visible band, greatly reducing their impact on the upscatter solar spectral irradiance. Although higher-order modes begin to appear at visible wavelengths for these sizes, their intensities are generally weaker than the dominant dipoles. To summarize the physical insights from Fig. 2 and 3, optimal particle design is primarily governed by the electric and magnetic dipole modes of the particle. Therefore, the Bond albedo can be maximized by tuning the dipolar modes to coincide with the peak of the solar spectral irradiance. After the material is selected and the refractive index of the particle is fixed, this is achieved by controlling particle size.

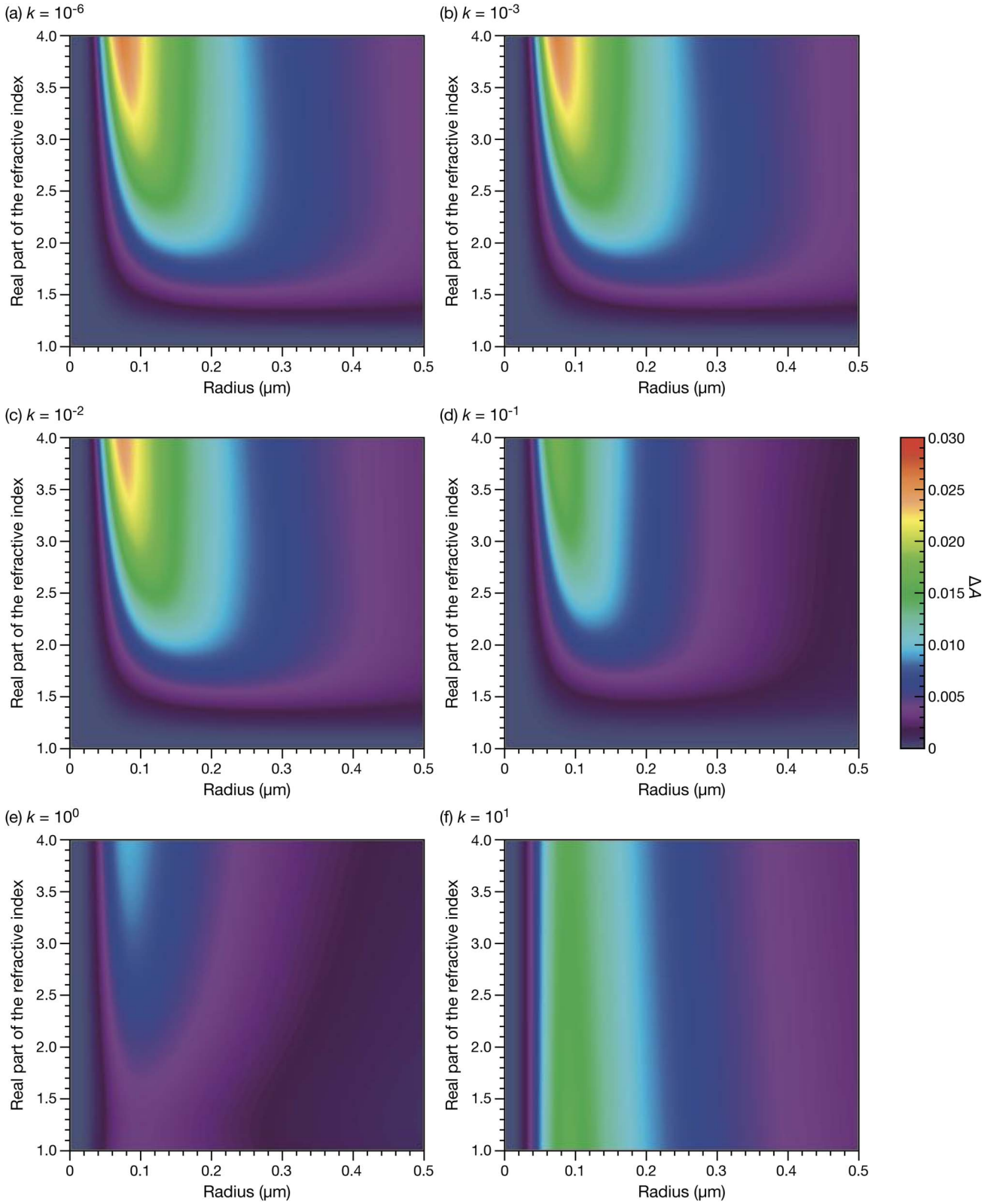

Fig. 5 The effect of imaginary part of the refractive index, k, on the change in the Bond albedo, ΔA, as a function of particle radius and the real part of the refractive index. The values of k are (a) 10^{-6}, (b) 10^{-3}, (c) 10^{-2}, (d) 10^{-1}, (e) 1, and (f) 10. The full solar spectrum is used in all calculations.

Fig. 4 shows how ΔA varies with particle radius for eight different materials that are candidates for SAI.[24] Each panel compares two calculations: one using a complex RI fixed at its value for $\lambda = 0.55$ μm (dotted lines) and the other incorporating a wavelength-dependent complex RI from 0.2 to 3.0 μm (solid lines). Rutile, anatase, and α-SiC exhibit the largest ΔA peaks,

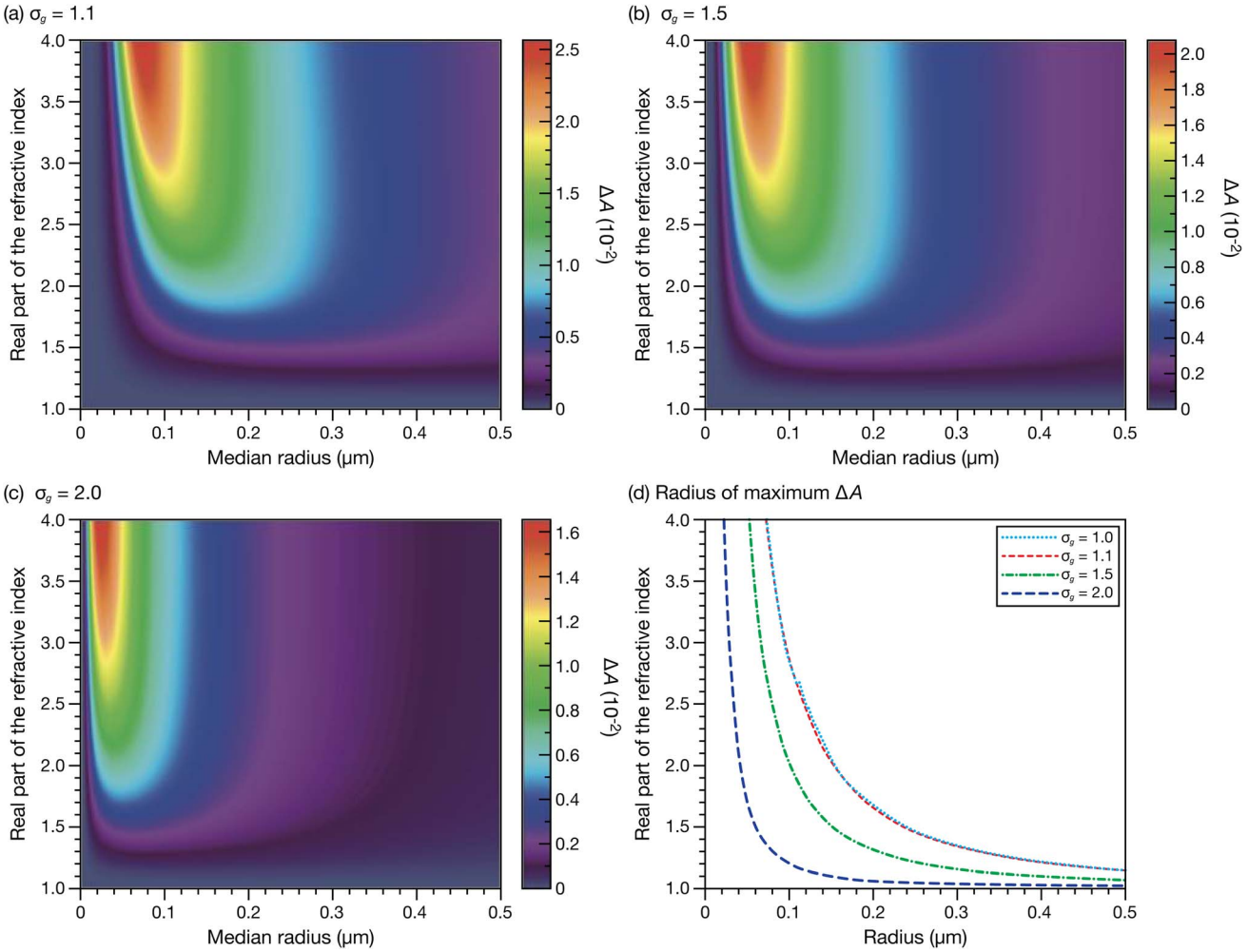

Fig. 6 The effect of a log-normal size distribution on the change in the Bond albedo, ΔA, as a function of median particle radius and the real part of the refractive index. In all calculations, the imaginary part of the refractive index is set to 10^{-9}. The values of the geometric standard deviation, σ_g, are (a) 1.1, (b) 1.5, and (c) 2.0. The full solar spectrum is used in all calculations. In (d), the position of the maximum ΔA for (a–c) is shown. The maximum of $\sigma_g = 1$, a monodisperse aerosol, is also presented in (d) for reference.

which is expected since these materials have the highest real part of the RI, n, in the visible region of the spectrum. They also show the most pronounced differences at their optimal radii when wavelength dependence is included, as n varies significantly in this region (Fig. S2). For the remaining materials, the discrepancy between the two calculations is negligible because n remains relatively constant across visible wavelengths. Overall, while the inclusion of dispersion is necessary for accurate calculations, it primarily acts as a first-order correction.

Fig. 5 shows the effect of the imaginary part of the RI, k, on ΔA as a function of particle radius and the real part of the RI. The full solar spectrum is used in all calculations. In Fig. 5a and b, where k is small ($k = 10^{-6}$ and $k = 10^{-3}$, respectively), the imaginary part of the RI has a negligible effect on the results, and the behavior is dominated by scattering. In Fig. 5c, as k increases past 10^{-2}, absorption becomes very significant, leading to noticeable decreases in ΔA across the heat map. This continues as k increases further (Fig. 5d and e) and ΔA is greatly reduced. However, when k becomes extremely large, as shown in Fig. 5f ($k = 10$), reflection begins to play a major role. This behavior corresponds to the case of a metallic material, where the real part of the dielectric function, $\varepsilon_1 = n^2 - k^2$, governs reflection by influencing the phase relationship between the incident and reflected waves at the interface. When ε_1 is negative, as is typical for metals at optical frequencies,[51] the RI becomes predominantly imaginary, leading to strong reflection and minimal transmission into the material. This arises because a negative ε_1 leads to a complex wave vector within the material, causing rapid attenuation of the transmitted wave and increased reflectance at the boundary. Consequently, as k increases beyond n reflection dominates over absorption and ΔA rises locally (of course, the strong infrared absorption of metallic nanoparticles would make them poor overall SAI candidates).

Fig. 6 shows the effect of particle size distribution on ΔA. Log-normal size distributions with three different geometric standard deviations (σ_g) are calculated as a function of median particle radius and refractive index, normalized to constant

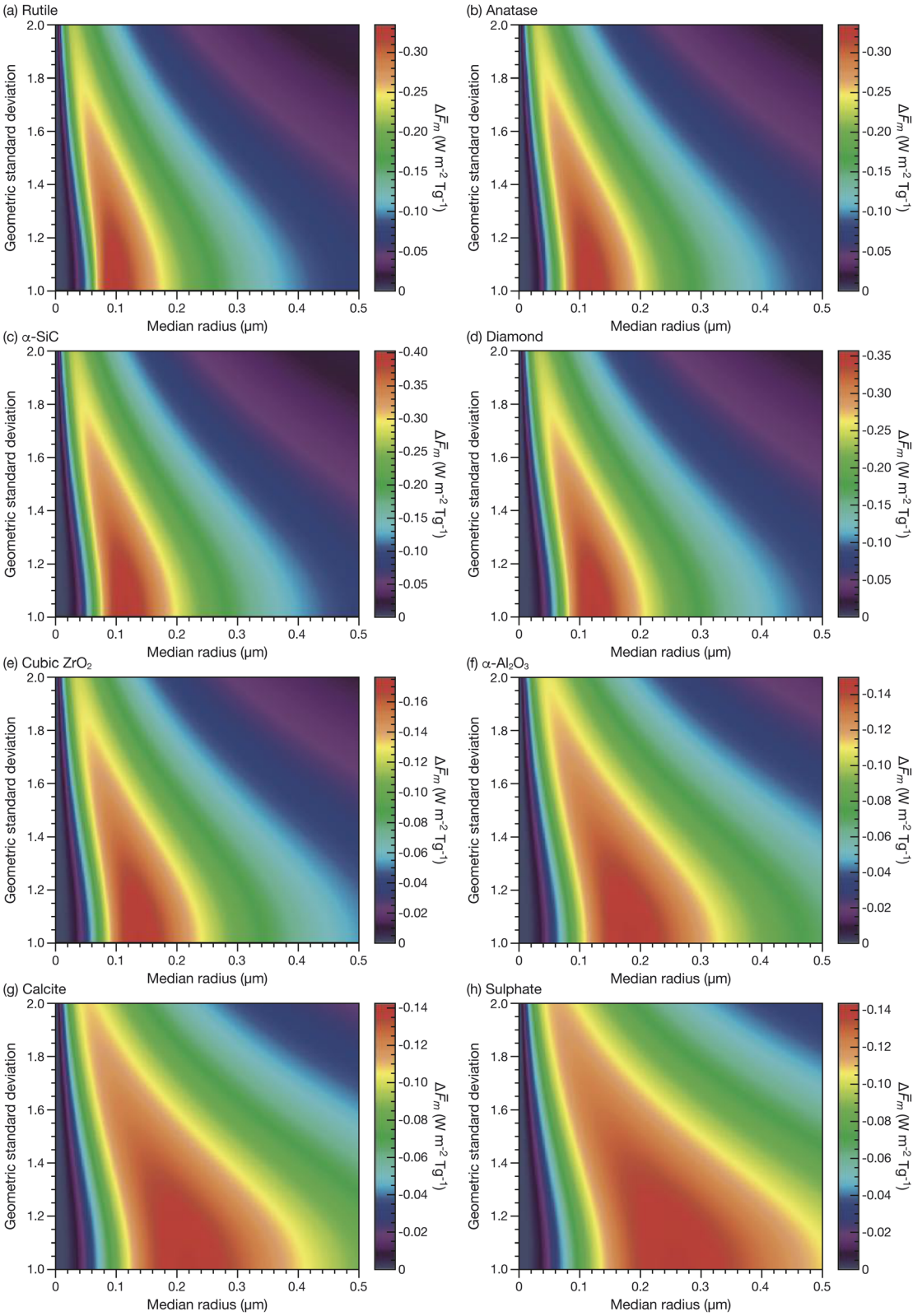

Fig. 7 Globally averaged radiative forcing per teragram, $\Delta\bar{F}_m$, of (a) rutile, (b) anatase, (c) α-SiC, (d) diamond, (e) cubic ZrO_2, (f) α-Al_2O_3, (g) calcite, and (h) sulphate aerosol particles as a function of median radius and geometric standard deviation of the particle size distribution. When calculating $\Delta\bar{F}_m$ for these materials, wavelength-dependent complex refractive index values between 0.2 and 3.00 μm and densities were taken from ref. 24 (the wavelength-dependent complex refractive index values are also shown in Fig. S2).

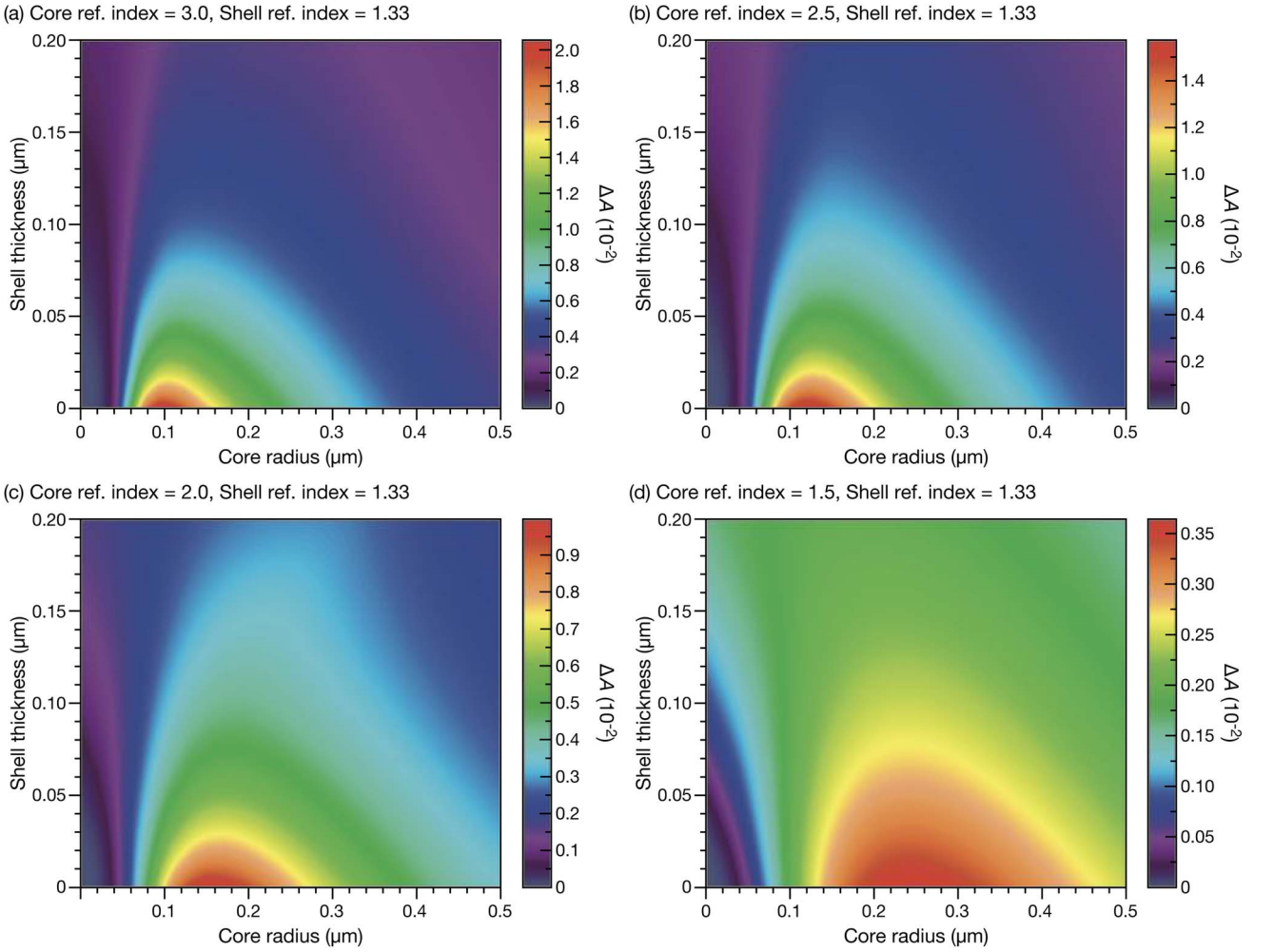

Fig. 8 The change in Bond albedo, Δ*A*, as the thickness of a layer of water changes on a spherical particle (the core). The values of the real part of the refractive index for the core are (a) 3.0, (b) 2.5, (c) 2.0, and (d) 1.5. The refractive index of the water layer (the shell) is 1.33. In all cases, the imaginary part of the refractive index is zero. The full solar spectrum is used in all calculations.

aerosol volume. Fig. 6a–c show (a) a narrow size distribution ($\sigma_g = 1.1$), (b) an intermediate size distribution ($\sigma_g = 1.5$), and (c) a broad size distribution ($\sigma_g = 2.0$). As the distribution width (σ_g) increases, the maximum Δ*A* decreases and shifts toward smaller median particle radii and lower refractive indices. Fig. 6d explicitly illustrates the radius at which the maximum Δ*A* occurs, highlighting that narrower distributions have larger optimal radii and higher refractive indices that yield maximum changes in albedo.

We next examine realistic parameter variations by combining wavelength-dependent complex RIs from the literature with varying log-normal size distributions. Fig. 7 plots the resulting globally averaged radiative forcing per teragram of injected aerosol, $\Delta\bar{F}_m$, for the eight candidate SAI materials considered in Fig. 4. For all materials, as the size distribution becomes more broad, $\Delta\bar{F}_m$ decreases and the optimal median radius shifts to lower sizes, following the trend seen in Fig. 6. The eight panels in Fig. 7 fall into two classes: the high real RI materials in panels (a–d) share very similar contour patterns and reach substantially larger cooling values than the intermediate-to-low real RI materials in panels (e–h), where $\Delta\bar{F}_m$ is less sensitive to the median particle radius. Material density also affects the results. The most striking example is cubic ZrO_2, which combines a relatively high real RI with the highest density of any of the eight materials (5.68 g cm^{-3}). Its greater mass per particle reduces the cooling achieved per teragram, explaining its weaker performance relative to purely optical expectations. For a realistic intermediate size distribution ($\sigma_g = 1.5$), the key takeaways are that in general: (i) optimal cooling with high real RI materials is more sensitive to the median radius than with low real RI materials, and (ii) optimizing the aerosol size distribution is more important than small increases in the real RI (for example, all high real RI materials exhibit similar cooling efficiencies).

The possibility that particles used for SAI become coated with water or sulfuric acid is a significant concern for the longevity and performance of the resulting aerosols. In the cold stratospheric environment, water vapor and sulfuric acid can condense onto the surface of particles, leading to changes in both size and composition.[23] This process not only produces

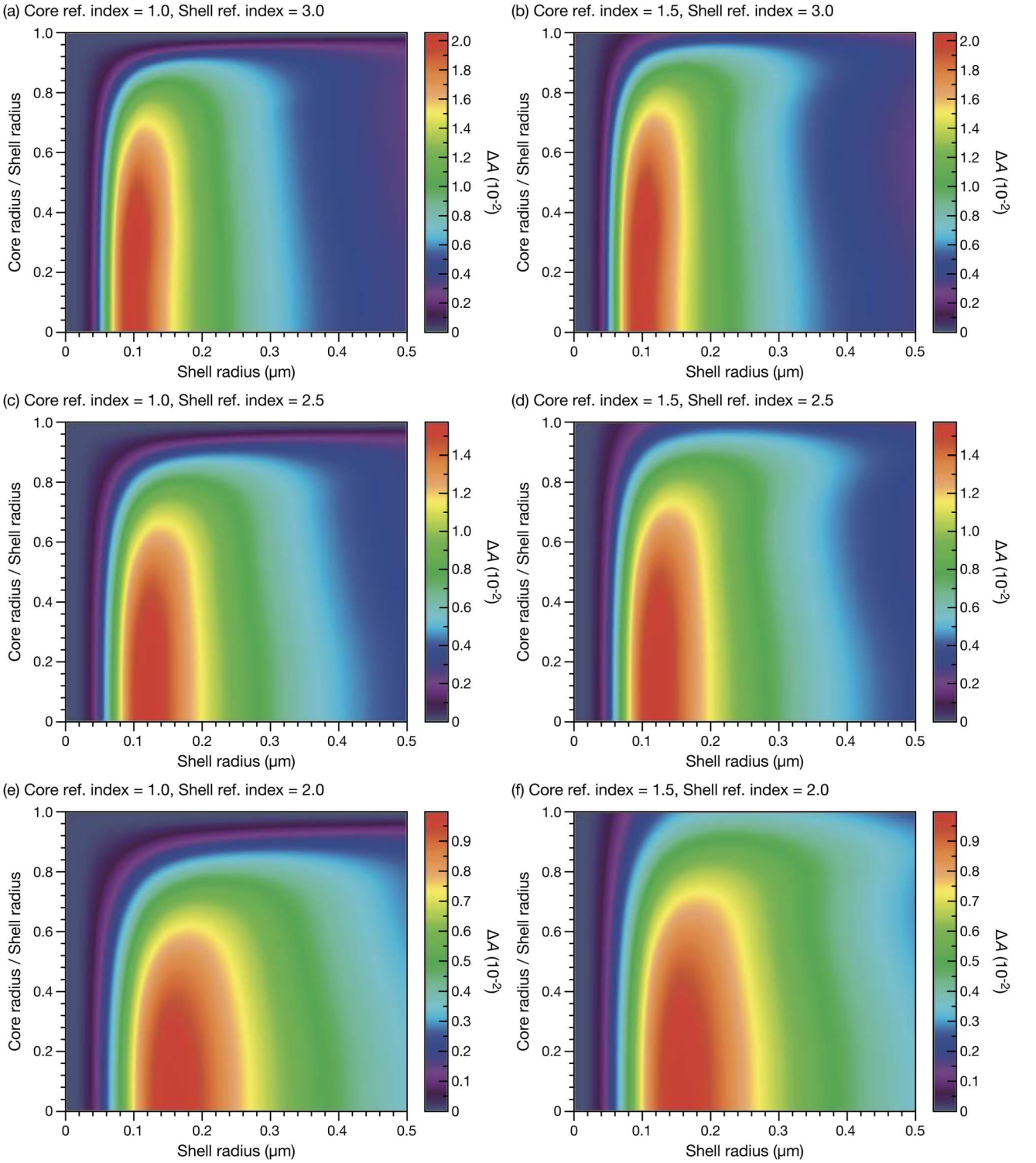

Fig. 9 The change in Bond albedo, Δ*A*, as a function of shell radius and the ratio of core radius to shell radius for different combinations of core and shell refractive indices. The values of the real part of the refractive index for the core and shell are (a) 1.0 and 3.0, (b) 1.5 and 3.0, (c) 1.0 and 2.5, and (d) 1.5 and 2.5, respectively. In all cases, the imaginary part of the refractive index is zero. The full solar spectrum is used in all calculations.

larger particles that sediment out of the stratosphere more rapidly but can also drastically alter how a particle scatters light. Fig. 8 shows how Δ*A* changes when a water layer of varying thickness (from zero to 0.20 μm) coats a spherical particle core of different radii and refractive indices. For high core refractive indices (*e.g.*, Fig. 8a), even a thin water coating on the order of several nanometres can spoil the optimized optical properties of SAI particles.

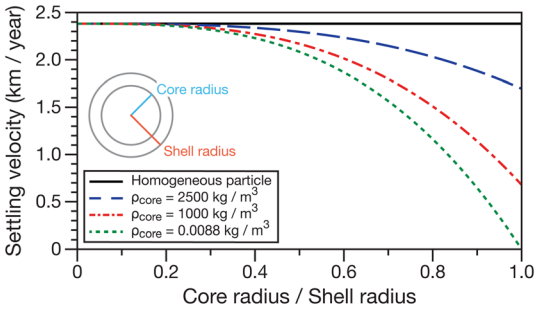

Fig. 10 Settling velocities of core–shell morphology particles with different core densities (ρ_{core}) as a function of the ratio of core radius to shell radius at 20 km altitude stratospheric conditions. All particles have a total radius of 0.1 μm and a shell density of 3510 kg m^{-3}. A homogeneous particle with a density of 3510 kg m^{-3} is shown in the black horizontal line. Settling velocities are calculated using the method described in ref. 37. Details are provided in the SI.

In general, core–shell structures provide additional parameters for optimizing particle properties in SAI (*i.e.*, through shell thickness and core–shell RI contrast). Fig. S3 illustrates the geometry of a core–shell particles. While the examples in Fig. 8 show that a lower real part of the RI shell can diminish ΔA, this is not the case for a higher real part of the RI shell. This is explored in Fig. 9, which provides several examples of how ΔA depends on both the thickness of a shell and its RI relative to that of a lower RI core. In all cases, the imaginary part of the RI is set to zero. First, comparisons between the left and right columns in Fig. 9 show that, except when the shell is very thin, the core's real part of the RI has little influence on ΔA, though a higher core RI can allow the shell to be thinner while preserving similar optical properties. Second, and more importantly, in all six panels, it is apparent that a higher RI shell enables ΔA to closely match that of a homogeneous particle; for instance, in Fig. 9a, at an outer radius of ~0.1 μm, ΔA is ~2 × 10^{-2} for a core-to-shell radius ratio of 0.5 and 0, the latter corresponding to a homogeneous sphere with a real part of the RI of 3.0. The design implications here are that a low-density core coated by a higher-density, higher real part of the RI shell can optically mimic a solid particle made entirely of the higher RI material. This offers a viable strategy for reducing overall particle mass while retaining the desired scattering properties.

To evaluate how core–shell design influences particle settling and stratospheric residence time, Fig. 10 shows the settling velocity for 0.10 μm radius, homogeneous particles with a density of 3510 kg m^{-3} (the density of diamond) and core–shell particles with a shell of the same density but varying core densities (ρ_{core}). These calculations follow the method from ref. 37 and are outlined in the SI. For a core-to-shell radius ratio of 0.5, where the optical properties of the homogeneous particle are preserved, the settling velocity can be reduced by about 12%. Much larger decreases are achievable; for example, increasing the core-to-shell radius ratio to 0.8 can lower the settling velocity by about 50%, although this also reduces ΔA relative to a fully homogeneous particle (see Fig. 9). Decreasing settling velocity to extend residence times reduces the required injection rate to sustain a given aerosol loading, potentially lowering operational costs and minimizing environmental impacts associated with continuous reinjection. However, these advantages must be balanced against other design requirements, such as

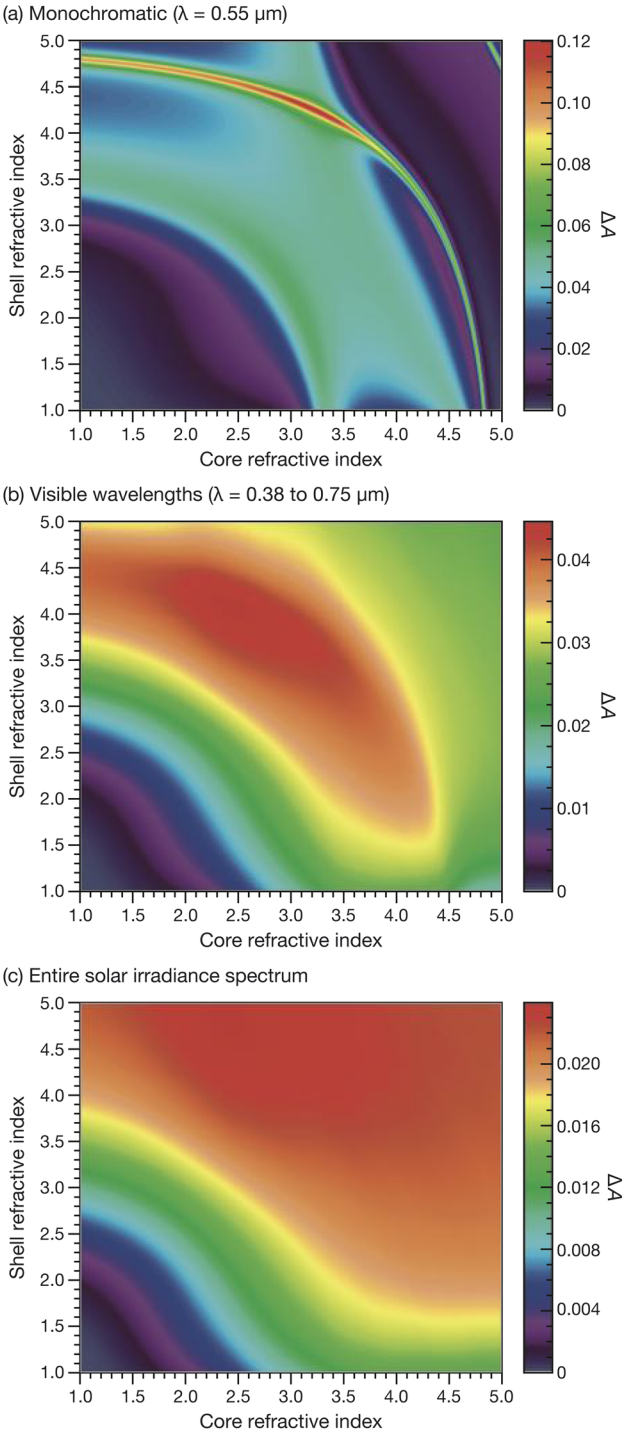

Fig. 11 Change in the Bond albedo, ΔA, in a core–shell particle as a function of real part of the core refractive index and the real part of the shell refractive index. In all cases, the shell radius is 0.1 μm, the ratio of core radius to shell radius is 0.8, and the imaginary part of the refractive index is zero. In (a), ΔA is calculated at $\lambda = 0.55$ μm, in (b) across $\lambda = 0.38–0.75$ μm, and in (c) over the full solar spectrum.

maintaining the shell's mechanical and chemical stability while preserving optimal optical properties. Core–shell and hollow metal oxide nanoparticle synthesis are documented in the literature.[52–54] By "decoupling" the desired optical performance (*via* a high-RI, high-density shell) from the gravitationally driven removal rate (*via* a low-density or hollow core), this core–shell approach offers a promising strategy for designing aerosols with both high scattering efficiency and prolonged stratospheric lifetimes.

An additional design question that emerges when examining core–shell structures is whether it is possible to achieve a higher ΔA than that of a homogeneous particle made of either the core or shell material alone. Fig. 11 illustrates the dependence of ΔA on core and shell RI for particles illuminated by (a) monochromatic light ($\lambda = 0.55$ μm), (b) visible wavelengths ($\lambda = 0.38$–0.75 μm), and (c) the full solar spectrum. Fig. 11a shows that substantial enhancements in ΔA are possible, most notably along a sharp red-orange ridge that spans a broad range of core RIs when combined with very high shell RIs (4.0–4.8). A weaker enhancement is also visible at lower shell RIs. However, as demonstrated previously in Fig. 1, illumination over a broad spectral range smooths and suppresses resonance features that dominate at single wavelengths. This effect is evident in Fig. 11b and c, where the enhancement in ΔA is significantly diminished and limited to extremely high shell RIs. Consequently, while composite materials can improve ΔA, the enhancement under broadband illumination remains modest for simple core–shell geometries (and requires shell RIs that are currently impractical). It may be possible that more complex composite particle structures can improve this situation, but that is beyond the scope of this work.

4 Summary

Within a light scattering framework assessing aerosol-induced changes to the Bond albedo, we present several findings relevant to SAI. Overlapping a particle's electric and magnetic dipolar resonances with the solar irradiance peak can significantly enhance reflectivity, particularly for radii around 0.10 μm. The magnitude of this enhancement depends primarily on the RI at the solar irradiance peak, although dispersion (wavelength-dependent RI variation) and absorption can also play a significant role. When realistic log-normal size distributions are considered, broadening shifts the optimal median radius downward and reduces ΔA. High RI materials such as rutile, anatase, α-SiC, and diamond exhibit similar cooling efficiencies across a range of particle size distributions when calculations span the full wavelength spectrum. This means that, once a sufficiently high RI is achieved, small differences in the RI are not that important, so the choice among these materials should instead prioritize chemical stability, low heterogeneous reactivity, photochemical robustness, toxicity, cost, ease of large-scale synthesis, minimal infrared absorption, compatibility with practical injection strategies, and the ability to produce and maintain the desired particle size distribution.

Beyond homogeneous spheres, even thin, low-RI coatings can diminish albedo gains. Therefore, understanding and mitigating particle growth from water or acid condensation is critical for evaluating both the efficacy and the side effects of SAI strategies. In contrast, core–shell particles that pair high RI shells with low-density cores preserve strong scattering while lowering particle mass and settling velocity. These results introduce engineered morphologies as a strategy for extending aerosol residence time in the stratosphere and optimizing material efficiency. The methodology developed here can be readily applied to more complex shapes and coatings, providing a rapid tool for evaluating new SAI particle formulations. Still, systematic laboratory measurements are needed to improve model predictions, while climate models incorporating improved aerosol optical data will clarify their viability.

Conflicts of interest

There are no conflicts to declare.

Data availability

The datasets generated from the calculations that are used to produce the figures in this study are available from the corresponding author upon request.

Sections S1–S3 and Fig. S1–S3. S1 compares bond albedo calculations using Mie and Henyey–Greenstein phase functions and provides formulae and a percent-error map (Fig. S1). S2 compiles the wavelength-dependent complex refractive indices used for eight candidate materials with the solar spectrum for reference (Fig. S2). S3 details the settling velocity model for core–shell particles at 20 km including governing equations, parameter values, and a geometry schematic (Fig. S3). See DOI: **https://doi.org/10.1039/d5ea00026b**.

Acknowledgements

All authors acknowledge financial support from the Simons Foundation (SFI-MPS-SRM-00005211).

References

1 P. Minnis, E. F. Harrison, L. L. Stowe, G. G. Gibson, F. M. Denn, D. R. Doelling and W. L. Smith, Radiative climate forcing by the Mount Pinatubo eruption, *Science*, 1993, **259**, 1411–1415.
2 M. P. Mccormick, L. W. Thomason and C. R. Trepte, Atmospheric effects of the Mt Pinatubo eruption, *Nature*, 1995, **2**, 399–404.
3 S. Self, Z. Jing-Xia, R. E. Holasek, R. C. Torres and J. King Alan, The atmospheric impact of the 1991 Mount Pinatubo, *NTRS-NASA Technical Reports 1*, 1993.
4 P. Heckendorn, D. Weisenstein, S. Fueglistaler, B. P. Luo, E. Rozanov, M. Schraner, L. W. Thomason and T. Peter, The impact of geoengineering aerosols on stratospheric temperature and ozone, *Environ. Res. Lett.*, 2009, **4**, 045108.
5 A. J. Ferraro, E. J. Highwood and A. J. Charlton-Perez, Weakened tropical circulation and reduced precipitation in

response to geoengineering, *Environ. Res. Lett.*, 2014, **9**, 014001.
6 A. C. Jones, J. M. Haywood and A. Jones, Climatic impacts of stratospheric geoengineering with sulfate, black carbon and titania injection, *Atmos. Chem. Phys.*, 2016, **16**, 2843–2862.
7 L. Xia, J. P. Nowack, S. Tilmes and A. Robock, Impacts of stratospheric sulfate geoengineering on tropospheric ozone, *Atmos. Chem. Phys.*, 2017, **17**, 11913–11928.
8 G. Pitari, V. Aquila, B. Kravitz, A. Robock, S. Watanabe, I. Cionni, N. Luca, G. Genova, E. Mancini and S. Tilmes, Stratospheric ozone response to sulfate geoengineering: Results from the geoengineering model intercomparison project (GeoMip), *J. Geophys. Res.*, 2014, **119**, 2629–2653.
9 W. Smith, U. Bhattarai, D. G. MacMartin, W. R. Lee, D. Visioni, B. Kravitz and C. V. Rice, A subpolar-focused stratospheric aerosol injection deployment scenario, *Environ. Res. Commun.*, 2022, **4**, 095009.
10 S. Tilmes, J. H. Richter, M. J. Mills, B. Kravitz, D. G. MacMartin, R. R. Garcia, D. E. Kinnison, J. F. Lamarque, J. Tribbia and F. Vitt, Effects of different stratospheric SO_2 injection altitudes on stratospheric chemistry and dynamics, *J. Geophys. Res. D: Atmos.*, 2018, **123**, 4654–4673.
11 M. Kuebbeler, U. Lohmann and J. Feichter, Effects of stratospheric sulfate aerosol geo-engineering on cirrus clouds, *Geophys. Res. Lett.*, 2012, **39**, L23803.
12 S. Tilmes, D. Visioni, A. Jones, J. Haywood, R. Séférian, P. Nabat, O. Boucher, E. M. Bednarz and U. Niemeier, Stratospheric ozone response to sulfate aerosol and solar dimming climate interventions based on the G6 Geoengineering Model Intercomparison Project (GeoMIP) simulations, *Atmos. Chem. Phys.*, 2022, **22**, 4557–4579.
13 S. Tilmes, R. R. Garcia, D. E. Kinnison, A. Gettelman and P. J. Rasch, Impact of geoengineered aerosols on the troposphere and stratosphere, *J. Geophys. Res. D: Atmos.*, 2009, **114**, D12305.
14 A. C. Jones, J. M. Haywood, N. Dunstone, K. Emanuel, M. K. Hawcroft, K. I. Hodges and A. Jones, Impacts of hemispheric solar geoengineering on tropical cyclone frequency, *Nat. Commun.*, 2017, **8**, 1382.
15 J. Proctor, S. Hsiang, J. Burney, M. Burke and W. Schlenker, Estimating global agricultural effects of geoengineering using volcanic eruptions, *Nature*, 2018, **560**, 480–483.
16 D. Visioni, D. G. Macmartin, B. Kravitz, O. Boucher, A. Jones, T. Lurton, M. Martine, M. J. Mills, P. Nabat, U. Niemeier, R. Séférian and S. Tilmes, Identifying the sources of uncertainty in climate model simulations of solar radiation modification with the G6sulfur and G6solar Geoengineering Model Intercomparison Project (GeoMIP) simulations, *Atmos. Chem. Phys.*, 2021, **21**, 10039–10063.
17 S. Vattioni, A. Stenke, B. Luo, G. Chiodo, T. Sukhodolov, E. Wunderlin and T. Peter, Importance of microphysical settings for climate forcing by stratospheric SO_2 injections as modeled by SOCOL-AERv2, *Geosci. Model Dev.*, 2024, **17**, 4181–4197.
18 R. C. Odoulami, M. New, P. Wolski, G. Guillemet, I. Pinto, C. Lennard, H. Muri and S. Tilmes, Stratospheric Aerosol Geoengineering could lower future risk of 'Day Zero' level droughts in Cape Town, *Environ. Res. Lett.*, 2020, **15**, 124007.
19 T. D. Patel, R. C. Odoulami, I. Pinto, T. S. Egbebiyi, C. Lennard, B. J. Abiodun and M. New, Potential impact of stratospheric aerosol geoengineering on projected temperature and precipitation extremes in South Africa, *Environ. Res.: Clim.*, 2023, **2**, 035004.
20 U. K. Krieger, J. C. Mössinger, B. Luo, U. Weers and T. Peter, Measurement of the refractive indices of h2so4–hno3–h2o solutions to stratospheric temperatures, *Appl. Opt.*, 2000, **39**, 3691–3703.
21 F. D. Pope, P. Braesicke, R. G. Grainger, M. Kalberer, I. M. Watson, P. J. Davidson and R. A. Cox, Stratospheric aerosol particles and solar-radiation management, *Nat. Clim. Change*, 2012, **2**, 713–719.
22 E. Wunderlin, G. Chiodo, T. Sukhodolov, S. Vattioni, D. Visioni and S. Tilmes, Side effects of sulfur-based geoengineering due to absorptivity of sulfate aerosols, *Geophys. Res. Lett.*, 2024, **51**, GL107285.
23 D. K. Weisenstein, D. W. Keith and J. A. Dykema, Solar geoengineering using solid aerosol in the stratosphere, *Atmos. Chem. Phys.*, 2015, **15**, 11835–11859.
24 J. A. Dykema, D. W. Keith and F. N. Keutsch, Improved aerosol radiative properties as a foundation for solar geoengineering risk assessment, *Geophys. Res. Lett.*, 2016, **43**, 7758–7766.
25 S. Vattioni, S. K. Käslin, J. A. Dykema, L. Beiping, T. Sukhodolov, J. Sedlacek, F. N. Keutsch, T. Peter and G. Chiodo, Microphysical interactions determine the effectiveness of solar radiation modification *via* stratospheric solid particle injection, *Geophys. Res. Lett.*, 2024, **51**, GL110575.
26 S. Vattioni, B. Luo, A. Feinberg, A. Stenke, C. Vockenhuber, R. Weber, J. A. Dykema, U. K. Krieger, M. Ammann, F. Keutsch, T. Peter and G. Chiodo, Chemical impact of stratospheric alumina particle injection for solar radiation modification and related uncertainties, *Geophys. Res. Lett.*, 2023, **50**, GL105889.
27 H. N. Huynh and V. F. McNeill, Heterogeneous reactivity of HCl on $CaCO_3$ aerosols at stratospheric temperature, *ACS Earth Space Chem.*, 2021, **5**, 1896–1901.
28 H. N. Huynh and V. F. McNeill, Heterogeneous chemistry of $CaCO_3$ aerosols with HNO3 and HCl, *J. Phys. Chem. A*, 2020, **124**, 3886–3895.
29 D. W. Keith, D. K. Weisenstein, J. A. Dykema and F. N. Keutsch, Stratospheric solar geoengineering without ozone loss, *Proc. Natl. Acad. Sci. U.S.A.*, 2016, **113**, 14910–14914.
30 C. H. Jackman, D. B. Considine and E. L. Fleming, A global modeling study of solid rocket aluminum oxide emission effects on stratospheric ozone, *Geophys. Res. Lett.*, 1998, **25**, 907–910.
31 H. N. Huynh and V. F. McNeill, The potential environmental and climate impacts of stratospheric aerosol injection: a review, *Environ. Sci.: Atmos.*, 2024, **4**, 114–143.
32 C. R. Usher, A. E. Michel and V. H. Grassian, Reactions on mineral dust, *Chem. Rev.*, 2003, **103**, 4883–4939.

33 J. Vukajlovic, J. Wang, I. Forbes and L. Šiller, Diamond-doped silica aerogel for solar geoengineering, *Diamond Relat. Mater.*, 2021, **117**, 108474.
34 P. Butzloff, *Reflective Hollow Srm Material and Methods International Patent*, WO 2022/094269 Al, 2022.
35 S. Vattioni, R. Weber, A. Feinberg, A. Stenke, J. A. Dykema, B. Luo, G. A. Kelesidis, C. A. Bruun, T. Sukhodolov, F. N. Keutsch, T. Peter and G. Chiodo, A fully coupled solid-particle microphysics scheme for stratospheric aerosol injections within the aerosol–chemistry–climate model SOCOL-AERv2, *Geosci. Model Dev.*, 2024, **17**, 7767–7793.
36 O. Coddington, J. L. Lean, D. Lindholm, P. Pilewskie and M. Snow, NOAA CDR Program, *NOAA Climate Data Record (CDR) of Solar Spectral Irradiance (SSI), NRLSSI Version 2.1*, 2017.
37 J. H. Seinfeld and S. N. Pandis, *Atmospheric Chemistry and Physics: from Air Pollution to Climate Change*, John Wiley & Sons, 2016.
38 W. J. Wiscombe and G. W. Grams, The backscattered fraction in two-stream approximations, *J. Atmos. Sci.*, 1976, **33**, 2440–2451.
39 C. F. Bohren and D. R. Huffman, *Absorption and Scattering of Light by Small Particles*, John Wiley & Sons, 2008.
40 A. L. Aden and M. Kerker, Scattering of electromagnetic waves from two concentric spheres, *J. Appl. Phys.*, 1951, **22**, 1242–1246.
41 M. I. Mishchenko, L. D. Travis and A. A. Lacis, Scattering, *Absorption, and Emission of Light by Small Particles*, Cambridge University Press, 2002.
42 D. R. Williams, *Earth Fact Sheet*, NASA Goddard Space Flight Center, National Space Science Data Center, **https://nssdc.gsfc.nasa.gov/planetary/factsheet/earthfact.html**, 2024, accessed 21 June 2025.
43 R. M. Bright and M. T. Lund, CO_2-equivalence metrics for surface albedo change based on the radiative forcing concept: a critical review, *Atmos. Chem. Phys.*, 2021, **21**, 9887–9907.
44 J. G. Shepherd, *Geoengineering the Climate: Science, Governance and Uncertainty*, Royal Society of London, 2009.
45 R. J. Charlson, J. Langner, H. Rodhe, C. B. Leovy and S. G. Warren, Perturbation of the northern hemisphere radiative balance by backscattering from anthropogenic sulfate aerosols, *Tellus A*, 1991, **43**, 152–163.
46 J. M. Haywood and K. P. Shine, The effect of anthropogenic sulfate and soot aerosol on the clear sky planetary radiation budget, *Geophys. Res. Lett.*, 1995, **22**, 603–606.
47 P. Forster, T. Storelvmo, K. Armour, W. Collins, J.-L. Dufresne, D. Frame, D. J. Lunt, T. Mauritsen, M. D. Palmer, M. Watanabe and M. Wild, The earth's energy budget, climate feedbacks, and climate sensitivity, in *Climate Change 2021: the Physical Science Basis. Contribution of Working Group I to the Sixth Assessment Report of the Intergovernmental Panel on Climate Change*, ed. Masson-Delmotte, V., Zhai, P., Pirani, A., Connors, S. L., Péan, C., Berger, S., Caud, N., Chen, Y., Goldfarb, L., Gomis, M. I., Huang, M., Leitzell, K., Lonnoy, E., Matthews, J. B. R., Maycock, T. K., Waterfield, T., Yelekçi, O., Yu, R. and Zhou, B., Cambridge University Press, Cambridge, UK and New York, NY, USA, 2021, pp. 923–1054, **https://www.ipcc.ch/report/ar6/wg1/chapter/chapter-7/**.
48 A. I. Kuznetsov, A. E. Miroshnichenko, M. L. Brongersma, Y. S. Kivshar and B. Luk'yanchuk, Optically resonant dielectric nanostructures, *Science*, 2016, **354**, aag2472.
49 Z.-J. Yang, R. Jiang, X. Zhuo, Y.-M. Xie, J. Wang and H.-Q. Lin, Dielectric nanoresonators for light manipulation, *Phys. Rep.*, 2017, **701**, 1–50.
50 B. Vennes and T. C. Preston, Quasinormal modes of spheroidal resonators in the null-field framework and application to hybrid anapoles, *Phys. Rev. A*, 2022, **106**, 013513.
51 P. B. Johnson and R. W. Christy, Optical constants of the noble metals, *Phys. Rev. B: Condens. Matter Mater. Phys.*, 1972, **6**, 4370–4379.
52 X. Wang, J. Feng, Y. Bai, Q. Zhang and Y. Yin, Synthesis, properties, and applications of hollow micro-/nanostructures, *Chem. Rev.*, 2016, **116**, 10983–11060.
53 R. H. A. Ras, M. Kemell, J. de Wit, M. Ritala, G. ten Brinke, M. Leskelä and O. Ikkala, Hollow inorganic nanospheres and nanotubes with tunable wall thicknesses by atomic layer deposition on self-assembled polymeric templates, *Adv. Mater.*, 2007, **19**, 102–106.
54 J. Zhao, M. Liu, J. Chang, Y. Shao, B. Liu and R. Liu, Al_2O_3 hollow nanospheres prepared by fluidized bed chemical vapor deposition and further heat treatment, *J. Am. Ceram. Soc.*, 2019, **102**, 6463–6468.